9-1-2013

Discovery of high-frequency iron K lags in Ark 564 and Mrk 335

E. Kara
Institute of Astronomy, Cambridge

A. C. Fabian
Institute of Astronomy, Cambridge

E. M. Cackett
Wayne State University, ecackett@wayne.edu

P. Uttley
Astronomical Institute 'Anton Pannekoek', University of Amsterdam

D. R. Wilkins
Institute of Astronomy, Cambridge

See next page for additional authors

Monthly Notices
of the
ROYAL ASTRONOMICAL SOCIETY

MNRAS **434,** 1129–1137 (2013)
Advance Access publication 2013 July 17

doi:10.1093/mnras/stt1055

Discovery of high-frequency iron K lags in Ark 564 and Mrk 335

E. Kara,[1]⋆ A. C. Fabian,[1] E. M. Cackett,[2] P. Uttley,[3] D. R. Wilkins[1] and A. Zoghbi[4,5]

[1]*Institute of Astronomy, Madingley Rd, Cambridge CB3 0HA, UK*
[2]*Department of Physics and Astronomy, Wayne State University, Detroit, MI 48201, USA*
[3]*Astronmical Institute 'Anton Pannekoek', University of Amsterdam, Postbus 94249, 1090 GE Amsterdam, the Netherlands*
[4]*Department of Astronomy, University of Maryland, College Park, MD 20742, USA*
[5]*Joint Space-Science Institute (JSI), College Park, MD 20742-2421, USA*

Accepted 2013 June 11. Received 2013 June 11; in original form 2013 March 30

ABSTRACT

We use archival *XMM–Newton* observations of Ark 564 and Mrk 335 to calculate the frequency-dependent time lags for these two well-studied sources. We discover high-frequency Fe K lags in both sources, indicating that the red wing of the line precedes the rest-frame energy by roughly 100 and 150 s for Ark 564 and Mrk 335, respectively. Including these two new sources, Fe K reverberation lags have been observed in seven Seyfert galaxies. We examine the low-frequency lag-energy spectrum, which is smooth, and shows no feature of reverberation, as would be expected if the low-frequency lags were produced by distant reflection off circumnuclear material. The clear differences in the low- and high-frequency lag-energy spectra indicate that the lags are produced by two distinct physical processes. Finally, we find that the amplitude of the Fe K lag scales with black hole mass for these seven sources, consistent with a relativistic reflection model where the lag is the light travel delay associated with reflection of continuum photons off the inner disc.

Key words: black hole physics – galaxies: active – X-rays: galaxies.

1 INTRODUCTION

The soft time lag (where soft band variations lag behind corresponding variations in the hard band) has revealed a new perspective through which to study the X-ray emission mechanisms of supermassive black holes. Since a tentative finding in Ark 564 (McHardy et al. 2007) and the first robust discovery in 1H0707−495 (Fabian et al. 2009), the soft lag has been detected in nearly 20 other Seyfert galaxies (e.g. de Marco et al. 2011; Emmanoulopoulos, McHardy & Papadakis 2011; Zoghbi & Fabian 2011; Cackett et al. 2013; De Marco et al. 2013; Fabian et al. 2013; Zoghbi et al. 2013) and one black hole X-ray binary (Uttley et al. 2011). Additionally, studying the high-frequency soft lag as a function of energy (as first done by Zoghbi, Uttley & Fabian 2011) has allowed us to directly compare the lag-energy spectrum with the time-integrated energy spectrum in order to understand which spectral component contributes to the lag at a particular energy (see Kara et al. 2013a for details).

Recently, the lag-energy spectrum has revealed the lag associated with the broad iron K line. This was first discovered in the bright Seyfert galaxy NGC 4151 by Zoghbi et al. (2012). In that work, they not only discovered the Fe K lag, but also used a frequency-resolved approach to show that at lower frequencies (i.e. longer time-scales), the rest-frame energy of the Fe K line lagged behind the continuum, while at higher frequencies (i.e. shorter time-scales from a smaller emitting region), the longest lag comes from the red wing of the Fe K line. This is consistent with relativistic reflection off the inner accretion disc, where the reflected emission lags the continuum roughly by the light travel time between the corona and the accretion disc.

An alternative interpretation has been proposed by Miller et al. (2010), in which the X-ray source is partially covered by optically thick clouds that are hundreds of gravitational radii from the source. In this case, the long, low-frequency hard lag is the reverberation between the source and the distant reflector, and the soft lag is simply the byproduct of taking the Fourier transform of the sharp-edged response function of clumpy reverberating material. This alternative interpretation has not yet been shown to be able to explain the observed broad Fe K lag at high frequencies. Furthermore, the soft lag has also been observed in an X-ray binary, where there is no evidence for distant circumnuclear material (Uttley et al. 2011).

Fe K lags have so far been observed in a total of five sources (Zoghbi et al. 2012, 2013; Kara et al. 2013a,b). In this paper, we present the discovery of the Fe K lag in two new sources, Ark 564 and Mrk 335. The two sources are X-ray bright and highly variable, making them the ideal candidates for spectral timing studies. The soft lag was first discovered in both of these sources by De Marco et al. (2013).

Ark 564 ($z = 0.0247$) was first observed with *XMM–Newton* in 2000/2001 at the beginning of the mission. In that short observation (10 ks of EPIC-pn exposure), the source was found to have a steep power law ($\Gamma \sim 2.5$) and large amplitude variability on short time-scales (Vignali et al. 2004). In 2005, the source was observed for 100 ks (Arévalo et al. 2006; Papadakis et al. 2007). McHardy et al.

⋆ E-mail: ekara@ast.cam.ac.uk

(2007) found that the power spectral density (PSD) of Ark 564 was well described by a power law with two clear breaks, similar to what is observed in Galactic black hole binaries in the soft state. The PSD was also well fitted by a two Lorentzian model, suggesting that the variability originates from two discrete, localized regions.

Most recently, Ark 564 was observed for 500 ks with *XMM–Newton*. Using this long observation, Legg et al. (2012) confirmed a significant soft lag between the 0.3–1 and 4–7.5 keV bands. This frequency-dependent time lag appeared narrower than in other sources, which led the authors to suggest a distant reflection origin. However, we must note that the lag spectrum was not computed between usual the soft, 0.3–1 keV, and medium, 1–4 keV, energy bands as is done in other sources.

Mrk 335 ($z = 0.0258$) is a remarkably variable source that has been observed in several different spectral states. Mrk 335 was observed for ∼130 ks in 2006 when the source was in a high flux interval (O'Neill et al. 2007; Larsson et al. 2008). Using this long observation, Arévalo, McHardy & Summons (2008) studied the timing properties of Mrk 335 and found that the PSD is well described by a broken power law, with a break at $\sim 10^{-4}$ Hz, corresponding to the frequency at which there was a sharp cut-off in the hard lag. They concluded that the frequency-dependent time lags were consistent with fluctuations propagating through the accretion flow. Recently, Gallo et al. (2013), using a 200 ks *XMM–Newton* obtained in 2009 (Grupe et al. 2012), showed that spectral and timing properties of this 200 ks observation were consistent with blurred reflection from an accretion disc around a rapidly spinning black hole ($a > 0.7$). Additionally, *Suzaku* observations of Ark 564 and Mrk 335 find high black hole spin for both objects using broad-band spectral fitting with relativistic reflection (Walton et al. 2013).

The paper is organized as follows. The observations and data reduction used in this analysis are described in Section 2. We review the Fourier method for calculating the lag in Section 3 and present the results in Section 4. Finally, we discuss the results in Section 5, and show how these results fit in with the growing sample of AGN with Fe K lags.

2 OBSERVATIONS AND DATA REDUCTION

For the analysis of these two sources, we use all of the archival data from the *XMM–Newton* observatory (Jansen et al. 2001), shown in Table 1. The data for both sources were reduced in the same way using the *XMM–Newton* Science Analysis System (SAS v.11.0.0) and the newest calibration files. We focus on the data from the EPIC-pn camera (Strüder et al. 2001) because of its faster readout time and larger effective area at high energies. The MOS data yield consistent results, but as the addition of the MOS data does not change or improve the overall lag spectra, they were not included in the analysis.

The data were cleaned for high background flares, and were selected using the conditions PATTERN $\leq$ 4 and FLAG ==0. The source spectra were extracted from circular regions of radius 35 arcsec centred on the maximum source emission. If pile-up was present, then an annular region was used to exclude the innermost source emission. Pile-up was an issue for some observations in Ark 564, and for consistency, we chose the same size excision radii used in Legg et al. (2012). The majority of the observations were taken in prime small window imaging mode, and for this mode, the background spectra were chosen from circular background regions, also of 35 arcsec radius. For observations taken in full window imaging mode (only the 2009 observations of Mrk 335), the background regions were made as large as possible, sometimes as large as twice the radius of the source region. The background subtracted light curves were produced with the tool EPICLCCORR. The light curves were all binned with 10 s bins.

3 THE FOURIER METHOD

To compute the time lags, we use the Fourier technique outlined in Nowak et al. (1999). This gives us time lags as a function of temporal frequency (i.e. time-scale^{-1}).

We start by generating light curves in different energy bands consisting of N observations in 10 s bins (i.e. $dt = 10$ s). The frequency range is limited at low frequencies by the length of the observation. The high-frequency cutoff is strictly the Nyquist frequency at $f = 1/(2dt)$; however, we are dominated by Poisson noise at frequencies well below the Nyquist frequency.

We take the discrete Fourier transform of each light curve. In this example, we will find the time delay between a soft band light curve, $s(t)$ and a hard band light curve, $h(t)$. The discrete Fourier transform of the soft band light curve is

$$\tilde{S}(f) = \frac{1}{N}\sum_{j=0}^{N-1} s(t_j)\mathrm{e}^{-2\pi \mathrm{i} f t_j/N},$$

where N is the number of time bins in the light curve, $s(t)$, and the frequency, $f = j/(Ndt)$. The soft band Fourier transform can

Table 1. The *XMM–Newton* observations used in this analysis. Columns show the source name, the observation ID, the start date, duration of the observation, net exposure time after live time correction and background flares, whether pile-up corrections were made, the observation mode and the size of the background region.

Object	Obs. ID	Obs. Date	Duration (s)	Exposure (s)	Pile up	Obs. mode	Bkg. reg. (arcsec)
Ark 564	0670130201	2011-05-24	59500	59100	Yes	sw	35
	0670130301	2011-05-30	55900	55500	No	sw	35
	0670130401	2011-06-05	63620	56820	No	sw	35
	0670130501	2011-06-11	67300	66900	Yes	sw	35
	0670130601	2011-06-17	60900	60500	No	sw	35
	0670130701	2011-06-25	64420	52620	No	sw	35
	0670130801	2011-06-29	58200	57800	Yes	sw	35
	0670130901	2011-07-01	55900	55500	Yes	sw	35
	0206400101	2005-01-05	98956	98660	No	sw	35
Mrk 335	0306870101	2006-01-03	133000	120000	No	sw	35
	0600540501	2009-06-11	80730	80700	No	fw	53
	0600540601	2009-06-13	130300	109820	No	fw	35

be written in the phasor form as the product of its amplitude and complex exponential phase is

$$\tilde{S}(f) = |\tilde{S}(f)|e^{i\theta_s}.$$

We take the Fourier transform of the hard band light curve, and then take its complex conjugate

$$\tilde{H}^*(f) = |\tilde{H}(f)|e^{-i\theta_h},$$

which reverses the sign of the phase. The product of $\tilde{S}(f)$ with the complex conjugate of the hard band, $H^*(f)$, is known as the cross-product $\tilde{C}(f)$ and is written as

$$\tilde{C}(f) = \tilde{H}^*\tilde{S} = |\tilde{H}||\tilde{S}|e^{i(\theta_s-\theta_h)}.$$

This gives the phase difference between the soft and the hard band. The overall Fourier phase lag, $\phi(f)$ is the phase of the average cross-power spectrum. That is,

$$\phi(f) = \arg[\langle\tilde{C}(f)\rangle].$$

The phase lag is then converted back into time to give us a frequency-dependent time lag between the two light curves:

$$\tau(f) \equiv \frac{\phi(f)}{2\pi f}.$$

It is important to note that the Fourier phase is defined on the interval $(-\pi, \pi)$, and therefore we are subject to phase wrapping, which causes the amplitude of the lag to change sign (Nowak et al. 1999). In other words, a constant lag of amplitude τ will change sign when $\phi = -\pi, \pi$ at the frequency $f = 1/(2\tau)$ (see Wilkins & Fabian 2013 for a more detailed discussion of phase wrapping).

3.1 The transfer function

An important step in understanding the origin of the lag is to characterize the linear transformation that relates two delayed light curves. This function, known commonly in signal processing as the impulse response function $t_r(\tau)$, relates the continuous hard and soft band light curves such that

$$s(t) = \int_{-\infty}^{\infty} t_r(t-\tau)h(\tau)d\tau.$$

The Fourier transform of the impulse response function is called the transfer function, $\tilde{T}_r(f)$.[1] The linear transformation between the soft and hard bands in the frequency domain is

$$\tilde{S}(f) = \tilde{T}_r(f)\tilde{H}(f).$$

Given this relation between the soft and hard bands, the cross-spectrum can just be written as

$$\tilde{C}(f) = |\tilde{H}(f)|^2\tilde{T}_r(f).$$

Therefore, the lag is derived from the phase of the transfer function. Theoretically, we should be able to directly measure the transfer function over a given frequency range by dividing the cross-spectrum by the hard band power spectrum. In practice, however, statistics are generally too low to allow a direct and unique measure of the transfer function using this method because calculating the transfer function requires a deconvolution of the signal in the two energy bands, which is known to enhance the noise level (see section 13.1 of Press et al. 1992 for further discussion of the deconvolution). Such analysis may be possible with future missions, such as *LOFT* or *Athena+*.

A common approach to studying the response function is to model the impulse response function (e.g. Reynolds et al. 1999) and compare the phase lag of the response function to the observed lags. This technique has been done by Wilkins & Fabian (2013) using general relativistic ray tracing simulations from the source, to the accretion disc and finally to the observer. In this inner disc reflection model, the hard lag is produced by a different mechanism (i.e. propagation effects through corona that cause the soft photons to respond before the hard photons). Therefore, the hard lags require a different response function. Miller et al. (2010) also used this technique of assuming a response function that fits the observed lag. They use a top-hat response function of length $\Delta\tau$ where $\Delta\tau$ corresponds to the maximum light travel delay between the X-ray source and a line-of-sight distant reflector. The sharp edge in this response function was shown to reproduce the high-frequency soft lag observed in a 500 ks observation of 1H0707−495.

3.2 Computing the lag-energy spectrum

The lag-energy spectrum is an important tool in directly comparing the lag with the time-integrated energy spectrum. We use the lag-energy spectrum as a way to see what parts of the spectrum contribute to the lag at specific frequencies.

The lag-energy spectrum is computed by measuring the frequency-dependent lag (described above) between the light curves of narrow energy bins ($\Delta E/E \sim 0.12$) and a reference band light curve (e.g. Zoghbi et al. 2011). The choice of reference band does not change the shape of the lag-energy spectrum, but it does change where the zero-point occurs. For this analysis, we chose the reference band to be the entire energy range, from 0.3 to 10. keV, excluding the small energy bin itself, so as not to have correlated errors (as discussed further in Zoghbi et al. 2013).

We note, therefore, that the interesting lag is not the absolute lag amplitude, but rather the relative lag between the energy bins. We read the lag-energy spectrum from bottom to top, the lower valued/more negative lag precedes the higher valued lag.

4 RESULTS

4.1 Ark 564

The light curves of Ark 564 in Fig. 1 show a bright and highly variable source over the 500 ks observation, making it a good candidate for searching for time lags. Fig. 2 shows the lag as a function of temporal frequency, using the technique described in Section 3. The top panel shows the lag between the soft band (0.3–1 keV) and a middle band (1.2–4 keV). The bottom panel shows the lag between the soft band and a hard band (4–7.5 keV), as first shown in Legg et al. (2012). Note the different scales on the *y*-axis. The two panels show different lag amplitudes, but the frequency of the soft lag is the same, independent of the amplitude of the hard lag. We note that the transition from positive to negative lag is not steep, as would be expected from an impulse response function with a sharp edge.

The amplitude of the lag between the soft and medium band is -95 ± 31 s at [3.5–4.5] $\times 10^{-4}$ Hz. Assuming a black hole

[1] The term 'transfer function' is often used in astronomy to describe the linear transformation in the time domain. However, according to conventional signal processing terminology, the 'transfer function' only refers to this linear transformation in the *frequency* domain. Therefore, strictly speaking, the 'transfer function' as typically known in astronomy, is actually called the 'impulse response function'. In this paper, we will adopt this correct terminology.

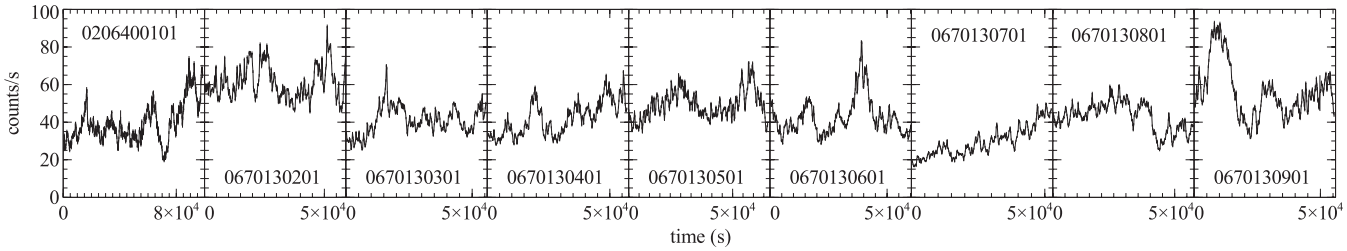

Figure 1. Ark 564 broad-band light curves from 0.3–10. keV in 200 s bins. For the purposes of comparing the counts rate between different observations, the light curves were all generated with circular source extraction regions with 35 arcsec radii. However, for the lag and spectral analysis, we accounted for pile-up by extracting annuli where needed. Note that the earlier observation (obsid 0206400101; leftmost panel) is longer, and is shown with a different x-axis scaling.

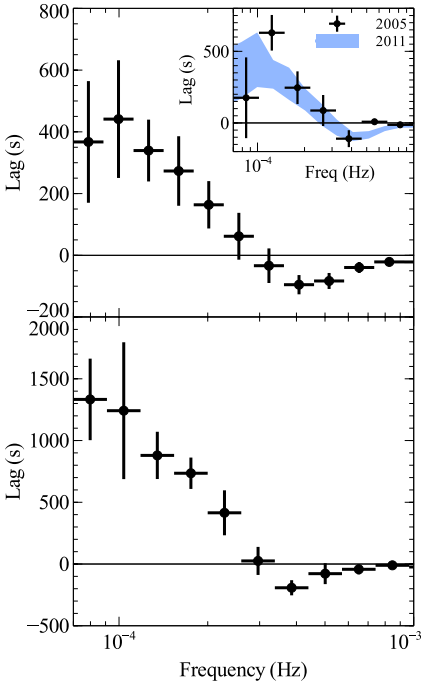

Figure 2. The lag as a function of temporal frequency for Ark 564. The lag is measured between 0.3–1 keV and 1.2–4 keV (top) and between 0.3–1 keV and 4–7.5 keV (bottom). The amplitudes of the soft and hard lags are much larger in the bottom panel. However, we note that the frequency of the soft lag is the same for both energy ranges. The inset shows the 0.3–1 to 1.2–4 keV lag using only the 100 ks observation from 2005 (black points) overlaid with the 1σ contours from the 2011 lag-frequency spectrum in blue. The 2005 soft lag is not significant, but is consistent with the new observations.

mass of $1.9 \times 10^6\,M_\odot$ (Zhang & Wang 2006), the amplitude and frequency of the soft lag are consistent with the black hole mass scaling relation of De Marco et al. (2013).

The inset in the top panel of Fig. 2 shows the lag between 0.3–1 and 1.2–4 keV using the 100 ks observation from 2005 in black points, overlaid with the 1σ contours of the 2011 lag-frequency spectrum in blue. The 2005 observation was taken when the source was in a similar flux regime. While the soft lag is not significant, it is consistent with the newer observations. The amplitude of the lag at $[3.5–4.5] \times 10^{-4}$ Hz is -140 ± 120 s, which is within error of the 2011 lag at the same frequency. The lag analysis for these data was first presented in McHardy et al. (2007), where they fitted a simple function across the entire high-frequency range. Using this technique, they estimated the amplitude of the soft lag between 0.5–2 and 2–8.8 keV to be -11.0 ± 4.3 s. The small amplitude and error of this lag is likely due to fitting for a constant lag across all

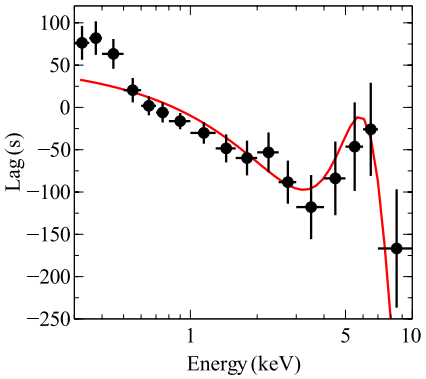

Figure 3. The lag-energy spectrum of Ark 564 in the frequency range $[3.2–5.2] \times 10^{-4}$ Hz. The lag-energy profile shows a peak at the energy of the Fe K line, and is similar to the soft lag-energy profiles seen in 1H0707−495 and IRAS 13224−3809. The red line shows the best-fitting linear model with an additional Gaussian at 6.4 keV.

the high frequencies, even where we see the lag is zero. Including this 100 ks observation into our analysis does not change the average lag-frequency spectrum or the lag-energy spectrum, and so we choose to present the results from only the four orbits from 2011, in order to make a direct comparison with the results presented in Legg et al. (2012).

The high-frequency lag-energy spectrum ($[3.2–5.2] \times 10^{-4}$ Hz) in Fig. 3 has the same general profile as the high-frequency lag-energy spectra seen in 1H0707−495 and IRAS 13224−3809. The high-energy lag spectrum is very similar to these other two sources, with a clear local maximum at 6 to 7 keV, the energy of the Fe K line and a dip at 3–4 keV. At 0.3–0.5 keV, we see a larger delay than in the other two sources, which may be indicative of ionization differences or more contribution from reprocessed blackbody emission from the irradiated accretion disc that causes a larger contribution of delayed emission relative to the direct emission.

As a check, we show the statistical significance of a model Gaussian to the feature at 6.4 keV. We fit a function to the data, $\tau(E) = a + bE + ce^{-(\frac{E-6.4}{d})^2}$, shown as the red line in Fig. 3. This function was modelled on the lag-energy spectra of 1H0707−495 and IRAS 13224−3809, where there are clear indications of a Fe K feature. We compared this model to one of just a line without the additional Gaussian. Comparing these two nested models yields an F-statistic, i.e. $\Delta\chi^2/\chi^2_\nu$, of 5.5.[2] Therefore, the Gaussian model is

[2] The F-test approach of testing for additive nested components where only the normalization is changed is standard for X-ray spectral fitting. Since we ensure that the normalization can be negative, we avoid the problem of fitting close to the parameter space boundary (Protassov et al. 2002)

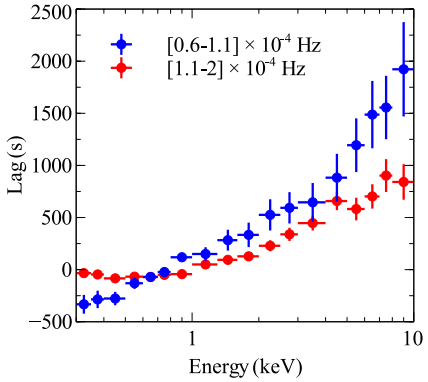

Figure 4. The low-frequency lag-energy spectrum of Ark 564 in the low-frequency range [0.6–1.1] $\times$ 10^{-4} Hz (blue) and [1.1–2] $\times$ 10^{-4} Hz (red). The profile is smooth and very different from the high-frequency lag-energy spectra.

preferred with 98.2 per cent confidence. We notice, however, that in this source, the 0.3–0.5 keV band diverges from a linear relation. If we avoid the soft excess, and only fit the functions between 0.5 and 10 keV, the Gaussian model is preferred with 99.94 per cent confidence.

In Fig. 4, we show the low-frequency hard lag dependence on energy for two slightly different frequency ranges. The lowest frequency range ([0.6–1] $\times$ 10^{-4} Hz in blue) shows a simple power-law shape, while the slightly higher frequency range ([1.1–2] $\times$ 10^{-4} Hz in red) is flat until 1 keV, when it turns upwards and follows the same power-law behaviour.

In the first reported results on this 500 ks observation of Ark 564, Legg et al. (2012) showed possible weak non-stationarity in the light curves from the first half of the observation (obsid 201–501) and the second half (obsid 601–901), taken a few weeks later. They reported a different frequency dependence of the soft lag and the PSD. Here, we report a slight difference in the lag-energy spectrum between the first and second halves of the observation (Fig. 5). The lag-energy spectrum of the first half of the observation (f = [3.4–4.5] $\times$ 10^{-4} Hz) shows a narrow lag feature peaking at 6–7 keV. The lag-energy spectrum of the second half of the observation covers a slightly larger range up to higher frequencies, f = [3.2–5.2] $\times$ 10^{-4} Hz, and shows a more constant behaviour, possibly with a peak at 4–5 keV. We note that the chosen energy bin size can affect the amplitude of the lag (i.e. averaging over larger energy bins will inevitably decrease the structure peaking at 6 to 7 keV). Nonetheless, using this finer binning, we find that the first half peaks at higher energies than the second half. The energy dependence seen here is reminiscent of the frequency-dependent lags in NGC 4151 that show a more narrow peak at low frequencies, and a broader feature at high frequencies (Zoghbi et al. 2012). No difference was found in the hard lag-energy spectra between the first and the second halves of the observation.

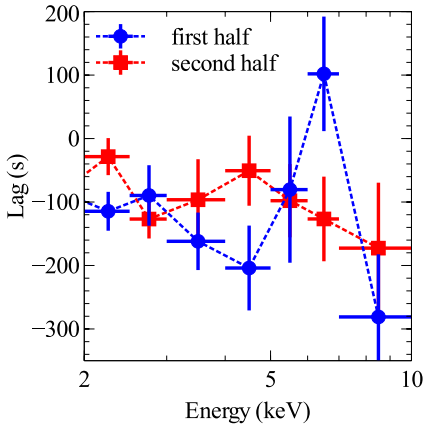

Figure 5. The lag-energy spectra of Ark 564 for the first half of the observation (obsid 201–501; blue) and the second half (obsid 601–901; red). The first half lag-energy spectrum is shown at ν = [3.4–4.5] $\times$ 10^{-4} Hz and the second half is shown at a slightly larger frequency range, ν = [3.2–5.2] $\times$ 10^{-4} Hz. The first half at lower frequencies clearly shows a narrower peak at 6 to 7 keV, while the second half at higher frequencies shows a broader feature peaking at 4 to 5 keV.

4.2 Mrk 335

Mrk 335 was observed in 2006 when it was very bright. Three years later, the source was observed again, this time while in a lower flux interval, with an average flux around 10 times less. The light curves in Fig. 6 show the 300 ks of observations taken in these dramatically different flux intervals.

We compute the lag as a function of frequency between 0.3–0.8 and 1.–4. keV for the 2006 observation of Mrk 335 (Fig. 7). The most negative lag is -155 ± 57 s at $f \sim 2 \times 10^{-4}$ Hz. We attempted to measure a lag in the lower flux observations from 2009, but no lag was found (inset of Fig. 7). The combined lag from all three observations (as shown in previous lag measurements of Mrk 335 in De Marco et al. 2013) is not significantly different than the lag presented in Fig. 7 because (1) the flux of the 2006 observation is much higher and therefore dominates the combined spectrum and (2) there is a constant zero lag measured in the low-flux observations, and therefore the shape of the lag-frequency spectrum does not change. In the low-flux observations from 2009, the lag in the same frequency range [1.9–7.6] $\times$ 10^{-4} Hz is measured to be -17.6 ± 81.0 s.

We isolate the frequencies [1.9–6.7] $\times$ 10^{-4} Hz in the high-flux observation from 2006 in order to look at the lag dependence on energy (Fig. 8). We find a lag of amplitude $\sim$150 s at the energy of the Fe K line. Using the same approach as for Ark 564, we fit the high-frequency lag-energy spectrum with two simple models: a line and a line plus a Gaussian at 6.4 keV (shown as the red line in Fig. 8). The line plus Gaussian model is preferred with $\sim$92 per cent (from an F-statistic of 3.6). Interestingly, even though Mrk 335 is known to have a stronger iron line than Ark 564, the detection of the Fe K lag is weaker in Mrk 335.

For completeness, we show the low-frequency lag-energy spectrum ([0.4–1.6] $\times$ 10^{-4} Hz) for the 2006 observation of Mrk 335 (Fig. 9). Similar to the low-frequency lag-energy spectrum of Ark 564 in Fig. 4, we find the low-frequency lag increases with energy. Though the error bars are larger for this source, it also appears to have a featureless low-frequency lag-energy spectrum.

5 DISCUSSION

The X-ray time lags from Seyfert galaxies have been explained mainly by two physical interpretations: relativistic reflection off the inner accretion disc and distant reflection from circumnuclear clouds. Both interpretations propose reflection of continuum photons to explain the broad iron line and the X-ray time lags. In the relativistic reflection model, the *short, high-frequency lags* are interpreted as reverberation between the continuum-emitting corona and the reflecting accretion disc (Fabian et al. 2009), and the low-frequency lags are produced by a different mechanism, consistent

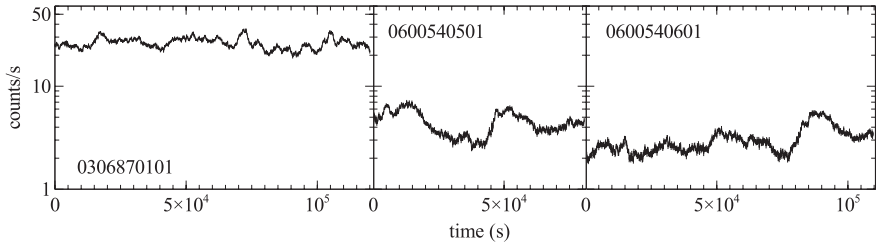

Figure 6. Mrk 335 broad-band light curve from 0.3–10. keV in 200 s bins. Note the logarithmic y-axis. The 2006 observation (left) is ∼10 times brighter than the 2009 observations (middle, right).

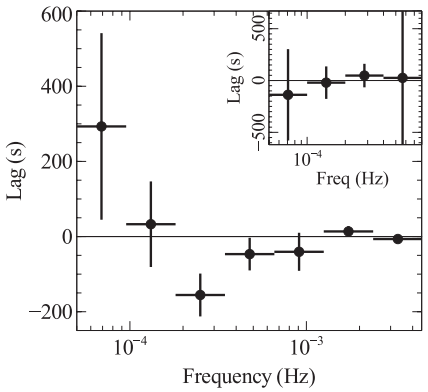

Figure 7. The Mrk 335 lag as a function of temporal frequency between 0.3–0.8 keV and 1–4 keV for the 2006 observations. The inset shows the lag as a function of frequency for just the 2009 low-flux observations. No lag was detected, and therefore we did not use these observations in the lag-energy analysis.

with propagating fluctuations in the disc that are transferred to the corona (Kotov, Churazov & Gilfanov 2001; Arévalo & Uttley 2006). In the partial covering model, it is the *long, low-frequency lags* that are interpreted as reverberation, now between the X-ray source and the distant reflector. In this model, the high-frequency lag is a mathematical artefact due to phase wrapping (Miller et al. 2010).

The high-frequency Fe K lags, as detected here in Ark 564 and Mrk 335 (Figs 3 and 8, respectively), are key to breaking the degeneracies between these two models. The broad Fe K line is an indicator of reflection in both models, however, we only observe a

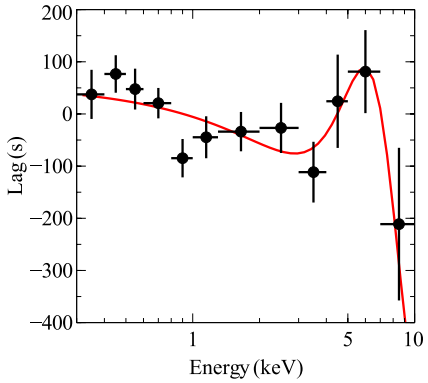

Figure 8. The Mrk 335 lag-energy spectrum in the frequency range [1.9–6.7] × 10^{-4} Hz. Only the data from 2006 were used as no lag was present in the 2009 observation. The red line shows the best-fitting linear model plus a Gaussian at 6.4 keV.

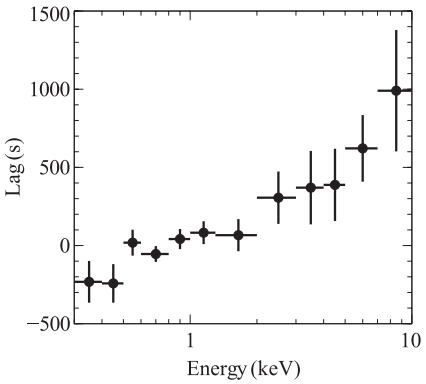

Figure 9. The low-frequency lag-energy spectrum of Mrk 335 in the low-frequency range [0.4–1.6] × 10^{-4} Hz. Like Fig. 4 the profile appears smooth and very different from the high-frequency lag-energy spectra.

Fe K reflection feature in the high-frequency lags, *not in the low-frequency lags* (i.e. Figs 4 and 9). In the case of partial covering, where the low-frequency lags are associated with reflection, it is not clear why the Fe K reflection feature is only seen at high frequencies. Furthermore, it is not clear how to reproduce the Fe K structure at high frequencies, if it is simply due to phase wrapping.

Variations of the partial covering model have been proposed to explain the lag-frequency spectrum of Ark 564 (using a small system of absorbing clouds at 100 r_g or less, modelled as a single top-hat response function; Legg et al. 2012) and for 1H0707−495 (using an extended wind from tens to hundreds of gravitational radii, modelled as several top-hat functions of different widths; Miller et al. 2010). While these different partial covering models can explain the lag-frequency spectra, neither has been shown to self-consistently explain the low- and high-frequency lag-energy spectra.

5.1 Partial covering view of lag-energy spectra

Here, we calculate the expected low- and high-frequency lag-energy spectra given the simple single top-hat response function, similar to the one concluded in Legg et al. (2012). In that work, the authors conclude that the lag-frequency spectrum between the soft band (0.3–1 keV) and the hard band (4–7.5 keV) can be explained as a single top-hat response function in the hard band lagging behind a delta function in both bands. The top panel of Fig. 2 shows the lag-frequency spectrum between the soft (0.3–1 keV) and medium bands (1–4 keV), which has a shorter low-frequency lag than the low-to-high lag-frequency spectrum, but has the same turnover frequency from hard-to-soft lags. This has been explained in the partial covering scenario of distant absorbers as a dilution effect (Miller et al. 2010). In this case, the source photons scatter through a medium whose opacity decreases with increasing

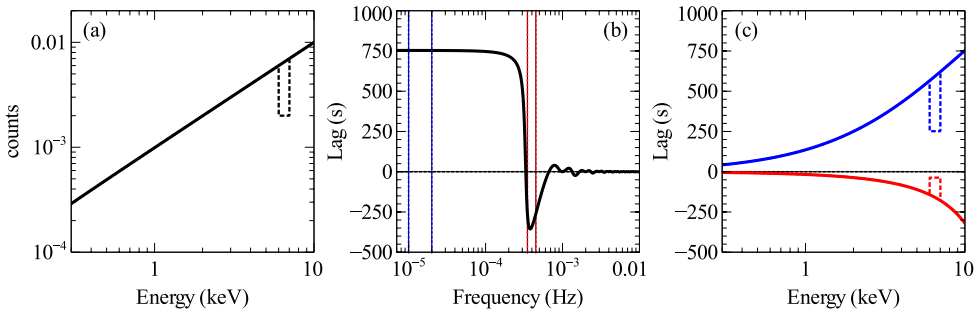

Figure 10. Model of the lag-energy spectra given a simple top-hat response function for two test cases: (1) where the reflection fraction increases steadily with energy (solid line) and (2) where the reflection fraction increases steadily with energy except for a demonstrative dip at 6 to 7 keV (dotted line). We show the reflection spectrum (a), the lag-frequency spectrum (b) and the low- and high-frequency lag-energy spectrum (c) shown in blue and red, respectively.

energy, and therefore the fraction of scattered photons increases with energy (as demonstrated by the top-hat response function whose amplitude increases with energy). This causes the amplitude of the low-frequency hard lag to increase with energy, but does not change the turnover frequency.

We illustrate this partial covering scenario in Fig. 10 by computing the lag-frequency spectrum and the low- and high-frequency lag-energy spectra for a single top-hat response function whose amplitude increases with energy. This assumes that the reflector's response to the direct emission is uniform over a distribution of time delays, with a width of $\Delta\tau$, and centred at t_0. For this demonstration, we choose $\Delta\tau = t_0 = 100$ s. The solid line in panel (a) shows the energy spectrum of the scattered light, steadily increasing with energy. We also include the case where the amplitude of the response function is not simply steadily increasing with energy (as shown by the dotted line with a clear feature at 6 to 7 keV). Panel (b) depicts the frequency-dependent lag between the direct emission and the reflected emission at 10 keV. Here, the soft lag is an artefact of taking the argument of the Fourier transform of the sharp-edge response function. The solid blue and red lines in panel (c) show the resulting lag-energy spectrum for low ([1–2] $\times$ 10^{-5} Hz) and high frequencies ([3.5–4.5] $\times$ 10^{-4} Hz), respectively. The increase in low-frequency lag with energy is a direct result of an increasing amount of dilution (i.e. an increasing fraction of scattered light). The high-frequency lag, as a relic of the hard lag, is therefore also affected by dilution, and we see a mirror image in the high-frequency lag-energy spectrum. We note that if the lag-energy dependence is due to a change in the width of the response function (rather than just a change in the amplitude as in the case presented here), the frequency turnover from hard-to-soft lags changes, and therefore causes a different shape to the high-frequency lag-energy spectrum that is not a mirror image of the hard lags. Given that in Ark 564 the turnover frequency from hard-to-soft lags does not change, we can rule out the possibility of a change in the width of the response function, but even still, this scenario does not reproduce the observed peak at 6.4 keV.

We have shown here that the response function proposed in Legg et al. (2012) can explain the low-frequency lag-energy spectrum (Fig. 4), but cannot reproduce the Fe K feature seen clearly in the high-frequency lag-energy spectrum (Fig. 3). We conclude that the high-frequency lag must have a different response function (and a different physical mechanism) from the low-frequency lag.

5.2 The growing sample of Fe K lags

High-frequency Fe K lags have now been discovered in seven Seyfert galaxies. Fig. 11 shows the lag-energy spectrum for four

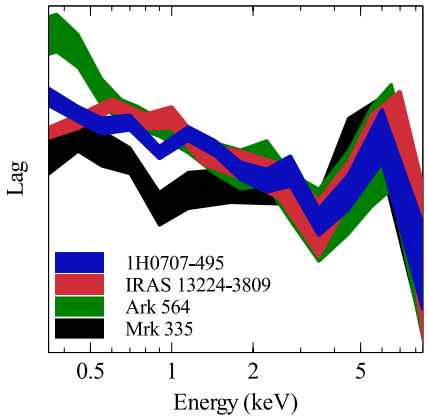

Figure 11. The high-frequency lag-energy profiles for four of the seven sources that exhibit Fe K lags, including 1H0707−495 (blue), IRAS 13224−3809 in at low fluxes (red), Ark 564 (green) and Mrk 335 (black). As the zero-point is arbitrary, the lags have been scaled to the 3 to 4 keV band. The Fe K lag profile is the same in all four sources, but the lags at the soft excess do not share a common shape.

of the seven sources (1H0707−495, IRAS 13224−3809, Ark564 and Mrk 335) with 68 per cent confidence contours. Since the zero-point is arbitrary and these sources have different lag amplitudes, the lag-energy spectra have been scaled to the 3 to 4 keV band. We focus on the overall shape, rather than the value of the lag. The four sources show very similar Fe K features, with a dip at 3 to 4 keV, a peak at 6 to 7 keV, and the most negative point at 8 to 10 keV. At lower energies, however, the lag-energy spectra diverge. There could be many reasons for this, including differences in iron abundance, ionization parameter, spectral index or blackbody temperature. Lags reveal a completely independent way of looking at the soft excess, and, with further work, could prove helpful in understanding the complexities of this energy band.

We plot the Fe K lag amplitude versus black hole mass for the seven sources (Fig. 12). The Fe K lag is measured between the 3–4 keV dip and the 6–7 keV peak. The black hole mass measurements were taken from the literature. Details can be found in Table 2. There is roughly a linear relationship between the amplitude of the lag and black hole mass, as expected by relativistic reflection. The light crossing times at 1 r_g and 6 r_g as a function of mass are shown as red and green lines, respectively, indicating that we are probing very close to the central black hole. We note that we do not account for the effect of dilution, and therefore, the intrinsic lag amplitudes are likely to be slightly larger than the observed lag. Also, we do not include the effect of the Shapiro delay, which is likely important close to the black hole (Wilkins & Fabian 2013). By comparing the

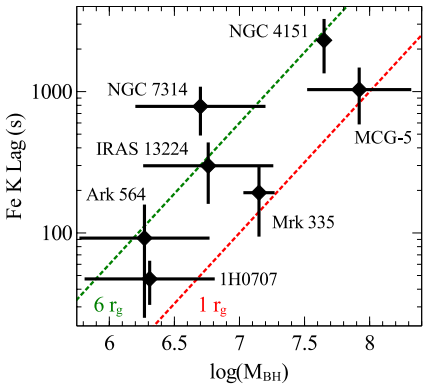

Figure 12. The amplitude of the Fe K lag versus $M_{\rm BH}$ for the seven Seyferts with detected Fe K reverberation lags. See Table 2 for details about the sources. The light crossing times at 1 $r_{\rm g}$ and 6 $r_{\rm g}$ as a function of mass are shown as red and green lines, respectively.

Table 2. Details of the black hole mass for the seven sources with an observed Fe K lag.

Object	log($M_{\rm BH}$)	$M_{\rm BH}$ reference
Ark 564	6.2 ± 0.5	Zhang & Wang (2006)
1H0707−495	6.31 ± 0.5	Bian & Zhao (2003)
NGC 7314	6.70 ± 0.5	Schulz, Knake & Schmidt-Kaler (1994)
IRAS 13224−3809	6.76 ± 0.5	Zhou & Wang (2005)
Mrk 335	7.15 ± 0.12	Peterson et al. (2004)
NGC 4151	7.65 ± 0.03	Bentz et al. (2006)
MCG-5-23-16	7.92 ± 0.4	Oliva et al. (1995)

lag at these high energies, we avoid complexities caused by the soft excess, but what is interesting, is that we still see the same mass scaling relation as found for the lags of the soft excess (De Marco et al. 2013). This points to a common origin of both the soft excess and the broad Fe K lag at small distances from the X-ray corona.

Lastly, we comment briefly on the apparent weak non-stationarity in the light curves (as noted by Legg et al. 2012, through the lag-frequency spectrum and PSD). Fig. 5 shows that the first half of the 500 ks observation peaks at the rest frame of the Fe K line, presumably from a larger emitting region, while at slightly higher frequencies, the second half shows a broader lag peaking at 4 to 5 keV, the red wing of the Fe K line from a smaller emitting region. While the non-stationarity of the light curves is not currently well understood, it does provide tantalizing evidence for further behaviour that will be accessible either through much deeper observations or future observatories.

The case for relativistic reflection continues to grow with recent discoveries of the Fe K reverberation lag (Zoghbi et al. 2012) that is now seen in seven sources, flux-dependent reverberation lags (Kara et al. 2013b), the black hole mass scaling relation with lag (De Marco et al. 2013), and reverberation lags in a black hole X-ray binary (Uttley et al. 2011) and possibly a neutron star (Barret 2013). The work presented here on Ark 564 and Mrk 335 support a relativistic reflection model and is not consistent with partial covering. The study of X-ray reverberation lags is quickly developing and is revealing a new perspective through which to probe strong gravity.

ACKNOWLEDGEMENTS

This work is based on observations obtained with *XMM–Newton*, an ESA science mission with instruments and contributions directly funded by ESA Member States and NASA. EK thanks the Gates Cambridge Scholarship. ACF thanks the Royal Society. The authors thank the anonymous referee for helpful comments.

REFERENCES

Arévalo P., Uttley P., 2006, MNRAS, 367, 801
Arévalo P., Papadakis I. E., Uttley P., McHardy I. M., Brinkmann W., 2006, MNRAS, 372, 401
Arévalo P., McHardy I. M., Summons D. P., 2008, MNRAS, 388, 211
Barret D., 2013, ApJ, 770, 9
Bentz M. C. et al., 2006, ApJ, 651, 775
Bian W., Zhao Y., 2003, MNRAS, 343, 164
Cackett E. M., Fabian A. C., Zogbhi A., Kara E., Reynolds C., Uttley P., 2013, ApJ, 764, L9
de Marco B., Ponti G., Uttley P., Cappi M., Dadina M., Fabian A. C., Miniutti G., 2011, MNRAS, 417, L98
De Marco B., Ponti G., Cappi M., Dadina M., Uttley P., Cackett E. M., Fabian A. C., Miniutti G., 2013, MNRAS, 431, 2441
Emmanoulopoulos D., McHardy I. M., Papadakis I. E., 2011, MNRAS, 416, L94
Fabian A. C. et al., 2009, Nat, 459, 540
Fabian A. C. et al., 2013, MNRAS, 429, 2917
Gallo L. C. et al., 2013, MNRAS, 428, 1191
Grupe D., Komossa S., Gallo L. C., Lia Longinotti A., Fabian A. C., Pradhan A. K., Gruberbauer M., Xu D., 2012, ApJS, 199, 28
Jansen F. et al., 2001, A&A, 365, L1
Kara E., Fabian A. C., Cackett E. M., Steiner J. F., Uttley P., Wilkins D. R., Zoghbi A., 2013a, MNRAS, 428, 2795
Kara E., Fabian A. C., Cackett E. M., Miniutti G., Uttley P., 2013b, MNRAS, 430, 1408
Kotov O., Churazov E., Gilfanov M., 2001, MNRAS, 327, 799
Larsson J., Miniutti G., Fabian A. C., Miller J. M., Reynolds C. S., Ponti G., 2008, MNRAS, 384, 1316
Legg E., Miller L., Turner T. J., Giustini M., Reeves J. N., Kraemer S. B., 2012, ApJ, 760, 73
McHardy I. M., Arévalo P., Uttley P., Papadakis I. E., Summons D. P., Brinkmann W., Page M. J., 2007, MNRAS, 382, 985
Miller L., Turner T. J., Reeves J. N., Braito V., 2010, MNRAS, 408, 1928
Nowak M. A., Vaughan B. A., Wilms J., Dove J. B., Begelman M. C., 1999, ApJ, 510, 874
Oliva E., Origlia L., Kotilainen J. K., Moorwood A. F. M., 1995, A&A, 301, 55
O'Neill P. M., Nandra K., Cappi M., Longinotti A. L., Sim S. A., 2007, MNRAS, 381, L94
Papadakis I. E., Brinkmann W., Page M. J., McHardy I., Uttley P., 2007, A&A, 461, 931
Peterson B. M. et al., 2004, ApJ, 613, 682
Press W. H., Teukolsky S. A., Vetterling W. T., Flannery B. P., 1992, Numerical Recipes. Cambridge Univ. Press, New York
Protassov R., van Dyk D. A., Connors A., Kashyap V. L., Siemiginowska A., 2002, ApJ, 571, 545
Reynolds C. S., Young A. J., Begelman M. C., Fabian A. C., 1999, ApJ, 514, 164
Schulz H., Knake A., Schmidt-Kaler T., 1994, A&A, 288, 425
Strüder L. et al., 2001, A&A, 365, L18
Uttley P., Wilkinson T., Cassatella P., Wilms J., Pottschmidt K., Hanke M., Böck M., 2011, MNRAS, 414, L60
Vignali C., Brandt W. N., Boller T., Fabian A. C., Vaughan S., 2004, MNRAS, 347, 854
Walton D. J., Nardini E., Fabian A. C., Gallo L. C., Reis R. C., 2013, MNRAS, 428, 2901
Wilkins D. R., Fabian A. C., 2013, MNRAS, 602
Zhang E.-P., Wang J.-M., 2006, ApJ, 653, 137
Zhou X.-L., Wang J.-M., 2005, ApJ, 618, L83

Zoghbi A., Fabian A. C., 2011, MNRAS, 418, 2642
Zoghbi A., Uttley P., Fabian A. C., 2011, MNRAS, 412, 59
Zoghbi A., Fabian A. C., Reynolds C. S., Cackett E. M., 2012, MNRAS, 422, 129
Zoghbi A., Reynolds C., Cackett E. M., Miniutti G., Kara E., Fabian A. C., 2013, ApJ, 767, 121

This paper has been typeset from a TEX/LATEX file prepared by the author.